Piezoelectric MEMS Energy Harvester for Low-Frequency Vibrations With Wideband Operation Range and Steadily Increased Output Power

Huicong Liu, Cho Jui Tay, Chenggen Quan, Takeshi Kobayashi, and Chengkuo Lee, *Member, IEEE*

***Abstract*—A piezoelectric MEMS energy harvester (EH) with low resonant frequency and wide operation bandwidth was designed, microfabricated, and characterized. The MEMS piezoelectric energy harvesting cantilever consists of a silicon beam integrated with piezoelectric thin film (PZT) elements parallel-arranged on top and a silicon proof mass resulting in a low resonant frequency of 36 Hz. The whole chip was assembled onto a metal carrier with a limited spacer such that the operation frequency bandwidth can be widened to 17 Hz at the input acceleration of 1.0 g during frequency up-sweep. Load voltage and power generation for different numbers of PZT elements in series and in parallel connections were compared and discussed based on experimental and simulation results. Moreover, the EH device has a wideband and steadily increased power generation from 19.4 nW to 51.3 nW within the operation frequency bandwidth ranging from 30 Hz to 47 Hz at 1.0 g. Based on theoretical estimation, a potential output power of 0.53 μW could be harvested from low and irregular frequency vibrations by adjusting the PZT pattern and spacer thickness to achieve an optimal design. [2010-0346]**

***Index Terms*—Low-frequency vibrations, microelectromechanical systems (MEMS), piezoelectric energy harvester, piezoelectric thin film (PZT), wideband.**

I. Introduction

In RECENT years, a great effort has been devoted to the study of self-powered electronics by using renewable power sources or energy scavengers to replace traditional batteries. Therefore, energy harvesting technique which is used to collect and convert ambient energy into usable electrical power has been considered as a promising solution and has attracted noticeable research interests [1]–[4]. Among many energy sources, vibration energy is ubiquitous in numerous applications ranging from common household devices, transportation tools, industry machines to human motions. In addition, vibration-based energy harvesters (EHs) using MEMS technology are reported to generate electricity based on piezoelectric, electromagnetic, electrostatic, and hybrid mechanisms [5]–[10]. Piezoelectric EHs convert mechanical strain into voltage output, i.e., electric field across the piezoelectric layer, based on the piezoelectric effect. Because of the advantages of simple configuration and high conversion efficiency, they have received much attention [11]–[15]. Currently, most investigations for power generation of vibration-based piezoelectric EHs focus on the configuration of cantilever beam with or without proof mass in the form of unimorph, series triple layer bimorph, parallel triple layer bimorph in the d_{31} mode and d_{33} mode [16]–[22]. However, the performances, such as output voltage and power, of piezoelectric EHs with piezoelectric elements in series or in parallel connections under similar mechanical strain conditions, have not been thoroughly studied.

A key challenge for vibration-based EH device is that it obtains the optimal power within a narrow frequency bandwidth nearby its resonant frequency. Away from the resonant frequency, the power generation drops dramatically and is too low to be utilized [23]. In fact, the frequencies of environmental vibration sources are relatively low (normally less than 200 Hz) and vary in a certain frequency range [2]. As a result, energy harvesting mechanisms which can respond to low-frequency vibrations with wideband operation range or tunable resonant frequency are considered to be promising solutions. Most reported MEMS-based piezoelectric EH devices operated at high resonant frequencies, which were more than 200 Hz or even exceed 1 kHz [24]–[34]. To the authors' best knowledge, there are no reported MEMS piezoelectric EHs realize low operation frequencies less than 50 Hz.

Zhu *et al.* [35] have reviewed and summarized many strategies to adjust or to tune the resonant frequency [36]–[41], or to widen the frequency bandwidth of the EH such that a generic EH can harvest energy from the ambient vibrations of different frequencies. Here, we mainly focus on the wideband approaches. Xue *et al.* [42] presented a wideband approach by integrating multiple piezoelectric bimorphs with different operation frequencies into a system. Comparing with single piezoelectric bimorph, analytic result showed a wideband power output for ten piezoelectric bimorphs in series with various thicknesses of piezoelectric layers. Seri *et al.* [43] reported a wideband electromagnetic EH by integrating series of cantilevers with different lengths and hence resonant frequencies.

Manuscript received December 12, 2010; revised May 6, 2011; accepted June 10, 2011. Date of publication September 1, 2011; date of current version September 30, 2011. This work was supported by a research grant of the University Research Fund R-263-000-475-112 and Academic Research Committee Fund MOE2009-T2-2-011 (R-263000598112) at the National University of Singapore. Subject Editor L. Lin.

H. Liu, C. J. Tay, and C. Quan are with the Department of Mechanical Engineering, National University of Singapore, Singapore 117576.

T. Kobayashi is with National Institute of Advanced Industrial Science and Technology (AIST), Tsukuba 305-8564, Japan.

C. Lee is with the Department of Electrical and Computer Engineering, National University of Singapore, Singapore 117576 (e-mail: elelc@nus.edu.sg).

Color versions of one or more of the figures in this paper are available online at http://ieeexplore.ieee.org.

Digital Object Identifier 10.1109/JMEMS.2011.2162488

This resulted in a wide operation frequency range of 4.2–5 kHz as well as an increased output power. Soliman *et al.* [44], [45] proposed a different wideband approach by using a mechanical stopper to change the stiffness of the resonator. The operation bandwidth of the EH can be increased 240% during frequency up-sweep. However, the authors only demonstrated a prototype of large size and did not show a real MEMS device. Nguyen *et al.* [46] presented a wideband MEMS electrostatic EH by utilizing nonlinear springs. The authors pointed out that the bandwidth increased by more than 13 times and the average harvesting output power increased by 68% compared to that of a linear vibration EH. Yang *et al.* [47] demonstrated a nonresonant electromagnetic energy harvesting mechanism by using a free-standing magnet packaged inside a sealed hole which is created by stacking five pieces of printed circuit board substrates embedded with multilayer copper coils. Most of the presented wideband approaches for energy harvesting only remain at prototype stage and only a few have realized in terms of MEMS devices [43], [46].

In this paper, we propose a microfabricated piezoelectric EH device which can realize a quite low resonant frequency as well as a wideband operation frequency range. In Section II, the device configuration and assembly strategy are illustrated, modeling of the voltage and power generation is discussed, and fabrication processes are presented. Furthermore, energy harvesting characterization and vibration measurement are performed and discussed in Section III. Then, output voltage and power of piezoelectric thin film (PZT) elements in series and parallel connections are studied. Finally, power evaluation and some recommendations for further improvement of the power generation are presented.

II. Design, Modeling, and Fabrication

A. Design and Configuration

Fig. 1(a) shows a schematic illustration of the MEMS-based piezoelectric energy harvesting cantilever (hereinafter called "piezoelectric cantilever") device operating in bending mode. The piezoelectric cantilever consists of a silicon proof mass (5 mm long $\times$ 5 mm wide $\times$ 0.4 mm thick) and a silicon supporting beam (3 mm long $\times$ 5 mm wide $\times$ 5 μm thick) integrated with ten parallel-arrayed PZT energy harvesting elements (hereinafter called "PZT elements"). For the convenience of illustration, the PZT elements are series assigned Arabic numbers from 1 to 10. The ten PZT elements are electrically isolated from one another and each PZT element is composed of a top electrode layer (Ti/Pt/Ti), a PZT layer, and a bottom electrode layer (Pt/Ti). Each of the top and bottom electrodes of the PZT element is connected to a bonding pad individually. The proof mass is designed and integrated at the end of the supporting beam to achieve a low resonant frequency of the cantilever. In Fig. 1(a), the proof mass undergoes an external excitation at a given acceleration resulting in the bending of the cantilever.

Fig. 1(b) illustrates the assembly strategy for the purpose of widening the operation frequency bandwidth of the piezoelectric cantilever. Narimani *et al.* [48] has reported an analytical modeling and experimental results of the frequency response of such single-degree-of-freedom piecewise linear oscillators.

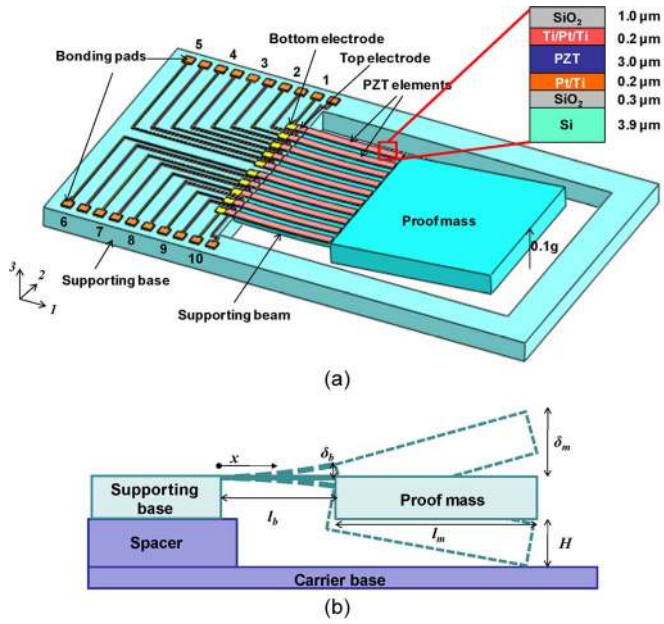

Fig. 1. (a) Schematic drawing of the piezoelectric cantilever with a large proof mass to gain in low resonant frequency. (b) Cross-section drawing of the piezoelectric cantilever regarding a spacer thickness designed properly for achieving wideband operation frequency.

According to the modeling and experimental results, oscillators with multistage stiffness result in a special case of frequency response, which is the frequency wideband response during frequency up-sweep. For the proposed piezoelectric cantilever, one approach to realize multistage stiffness is to adjust the spacer thickness between the proof mass and carrier base during assembly. As shown in Fig. 1(b), for a low external excitation, the piezoelectric cantilever vibrates freely at certain vibration amplitude. As the input acceleration increases to a certain level, the amplitude of half cycle δ_m for upward bending is increased. However, the amplitude of the other half cycle for downward bending is retarded by the carrier base to H. Therefore, the structure stiffness is changed at this stage, and the frequency bandwidth can be widened as the frequency sweeping up in the neighborhood of resonant frequency. According to steady-state response analysis by using Abaqus, the spacer thickness H between the proof mass and carrier base is designated as 1150 μm to realize stiffness change in the case that the acceleration is above 0.2 g. In other words, the bottom edge of proof mass will hit the carrier base surface when the acceleration of excitation vibration is higher than 0.2 g.

B. Modeling of Voltage and Power Generation

Considering such piezoelectric cantilever operating in 31 mode, meaning the mechanical stress/strain applies in axial direction (1-direction) and electrical field/displacement generates in transverse direction (3-direction), the piezoelectric constitutive equation is described as

$$D_3 = \varepsilon_{33} E_3 + d_{31}\sigma_1 \tag{1}$$

$$\xi_1 = s_{11}\sigma_1 + d_{31} E_3 \tag{2}$$

where ξ_1 and σ_1 are the axial mechanical strain and stress; E_3 and D_3 are the transverse electric field and electric

displacement; s_{11}, ε_{33}, and d_{31} denote the axial elastic compliance at a constant electric field, the transverse dielectric coefficient measured at a constant stress, and the transverse-axial piezoelectric constant.

According to (1) and (2), the applied mechanical strain induces an electric displacement in the piezoelectric layer. Meanwhile, an electric field develops across the electrodes in the thickness direction and sends feedback to the mechanical domain thus affecting the mechanical strain. As the piezoelectric cantilever is connected to an external electric circuit and the load resistance is increased from zero to infinity, the system changes from short-circuit to open-circuit conditions. For the calculation of short-circuit current, it is assumed that $E_3 = 0$; while for the calculation of open-circuit voltage, it is assumed that $D_3 = 0$ [21], [49]. Therefore, by having $V_{o.c.} = E_3 \cdot t_e$ and assuming a constant electric field in the thickness direction of the piezoelectric layer, the open-circuit voltage generated across the piezoelectric electrodes can be obtained from $E_3 = -d_{31}\sigma_1/\varepsilon_{33}$ and is expressed in terms of the mechanical strain distribution $\xi_1(x)$ along the PZT element as

$$V_{o.c.} = -\frac{1}{1-k^2}\frac{d_{31}Yt_e}{\varepsilon_{33}l_b}\int_0^{l_b}\xi_1(x)dx \tag{3}$$

where l_b is the length of supporting beam; t_e is the PZT thickness; $Y = 1/s_{11}$ is the Young's modulus of piezoelectric material; k is the electromechanical coupling coefficient (effect of strain on the electric field through the thickness of the piezoelectric layer [50]) defined by

$$k^2 = Yd_{31}^2/\varepsilon_{33}. \tag{4}$$

The strain distribution $\xi_1(x)$ along each PZT element refers to the strain distribution along the top surface of the supporting beam. Considering the cantilever is subjected to a base acceleration, since the supporting beam is ended with an extended proof mass, a concentrated force is assumed to be applied at the middle of the mass. When the beam bends, the PZT thin film layer at the surface of the supporting beam is stretched or compressed in the axial direction. The strain distribution $\xi_1(x)$ of the PZT layer in terms of the mass tip displacement δ_m is given as [21]

$$\xi_1(x) = \frac{3t_b}{l_b}\left(\frac{2l_b + l_m - 2x}{4l_b^2 + 9l_bl_m + 6l_m^2}\right)\delta_m \tag{5}$$

where variable x is the position along the supporting beam, and it refers to the distance starting from the beam anchor point and ending at the beam-mass connection point; l_b and l_m are the supporting beam length and proof mass length, respectively; t_b is the supporting beam thickness. Substituting (5) into (3), the overall open-circuit voltage of each PZT element related to the mass tip displacement is derived as

$$V_{o.c.} = -\frac{1}{1-k^2}\frac{d_{31}Yt_e}{\varepsilon_{33}l_b}\frac{3(l_b+l_m)t_b}{4l_b^2 + 9l_bl_m + 6l_m^2}\delta_m. \tag{6}$$

The average power delivered to the connected load Z_L is

$$P_{rms} = \frac{1}{2}\frac{|V_{o.c.}|^2}{|Z_P + Z_L|^2}\mathrm{Re}\{Z_L\} \tag{7}$$

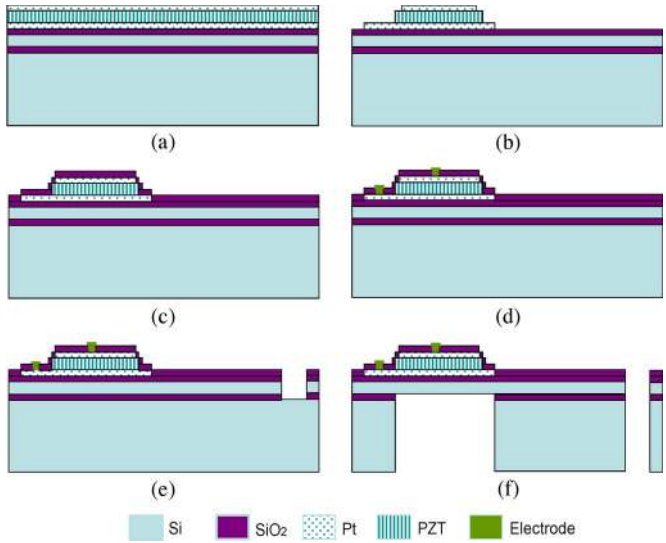

Fig. 2. Fabrication process. (a) Deposition of multiple layers of Ti/Pt/Ti/PZT/Pt/Ti/SiO_2. (b) Patterning of PZT elements. (c) Sputtering of SiO_2. (d) Patterning of Pt electrodes and metal lines. (e) Cantilever patterning. (f) Release of cantilever and proof mass.

where Z_P is the complex impedance of the PZT element. The maximum power occurs when the load impedance Z_L matches the complex conjugate of the PZT element, i.e., $Z_L = Z_P^*$. If the connected load is purely real, i.e., $Z_L = R_L$, the maximum average power occurs when the load matches the impedance magnitude of the PZT element, i.e., $R_L = |Z_P|$ and can be derived as

$$P_{rms} = \frac{1}{4}\frac{|V_{o.c.}|^2}{|Z_P| + \mathrm{Re}\{Z_P\}}. \tag{8}$$

C. Fabrication Process and Assembly

The microfabrication process of the piezoelectric cantilever was started from a silicon-on-insulator (SOI) wafer with Si structural layer of 5 μm, buried oxide layer of 1 μm, and Si handle layer of 400 μm. As shown in Fig. 2(a), after a thermal oxide (SiO_2) layer was deposited on the Si structural layer, multiple layer depositions of Pt/Ti bottom electrode layer, 3 μm thick (100)-oriented PZT thin film layer, and Ti/Pt/Ti top electrode layer were followed by sputtering, sol–gel, and sputtering processes, respectively [51]–[53]. Fig. 2(b) shows the Ti/Pt/Ti top electrodes, and Pt/Ti bottom electrodes were etched by Ar-ion beam while PZT thin films were wet-etched by an aqueous solution of HNO_3, HF, and HCl. After etching of the Ti/Pt/Ti/PZT/Pt/Ti multilayer, a SiO_2 layer was deposited by RF-magnetron sputtering acting as an insulation layer shown in Fig. 2(c). In Fig. 2(d), contact holes were created on the deposited SiO_2 layer by reactive ion etching (RIE) using CHF_3 gas. Subsequently, 1 μm thick Pt wires with Ti adhesion layer were deposited by sputtering and patterned to connect the top and bottom electrodes to bonding pads. In Fig. 2(e), the thermal oxide layer, structural Si layer, and buried oxide layer were etched by RIE with feed gases of CHF_3, SF_6, and CHF_3, respectively. Finally, Fig. 2(f) shows that the handle Si layer and buried oxide layer were etched from the backside to

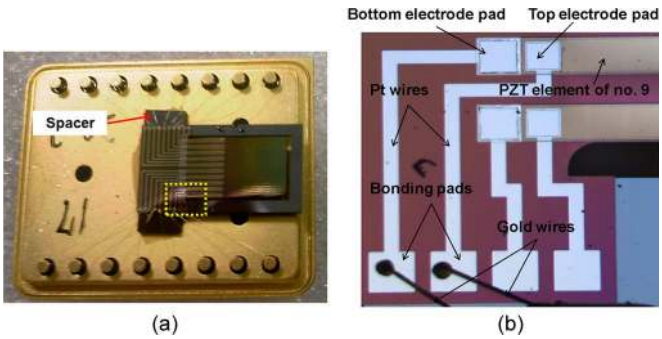

Fig. 3. (a) Microfabricated piezoelectric cantilever device assembled with DIP. (b) Optical microscope photo of two PZT elements connected with electrodes and bonding pads.

release the cantilever and proof mass structures. After that, the microfabricated piezoelectric cantilever device was assembled onto a dual in-line package (DIP) with a spacer chip of 1150 μm thick embedded in between the device and DIP. The gold wires were bonded from bonding pads of the device to metal pins of the DIP, as shown in Fig. 3(a). Fig. 3(b) shows the optical microscope view of the highlighted area of the piezoelectric cantilever in Fig. 3(a).

III. Dynamic Characteristics and Energy Harvesting

A. Testing Setup

In Fig. 4(a), a vibration testing system is employed for the energy harvesting measurement of the piezoelectric cantilever. It consists of an electromagnetic shaker, a power amplifier, a dynamic signal analyzer (DSA), an accelerometer, and its controller. The piezoelectric cantilever and the accelerometer are assembled onto the shaker. The vibration frequency and amplitude of the shaker are controlled by the DSA through the amplifier with an input sinusoidal signal. The output voltage of the piezoelectric cantilever is collected and recorded via the DSA through channel 1. The acceleration signal is collected into channel 2 and recorded to the DSA through the acceleration controller. Fig. 4(b) shows the equivalent voltage measurement circuit for one PZT element connected to the DSA. A PZT element can be considered as an AC voltage source V_S in series with a piezoelectric impedance Z_P. By using an impedance analyzer, the piezoelectric impedance Z_P is measured to be a capacitance C_P of 2.2 nF and a resistance R_P of 67.2 MΩ connected in parallel. Z_L is the input impedance of the DSA, which can be simplified as a resistance R_L of 1 MΩ. It is found that the magnitude of the piezoelectric impedance $|Z_P|$ is larger than the load resistance R_L of the DSA. Therefore, the output voltage detected by the DSA is not the open-circuit voltage V_S of the PZT element, but the load voltage V_L on the resistance R_L of the DSA. Therefore, unless special statement, the load rms voltage measured by DSA is considered as the load voltage delivered to the resistor of 1 MΩ.

To accurately characterize the vibration behavior of the piezoelectric cantilever, an optical method as shown in Fig. 5 is deployed. The optical measurement setup consists of a function generator, a DSA, a laser source with an angle adjustable tripod.

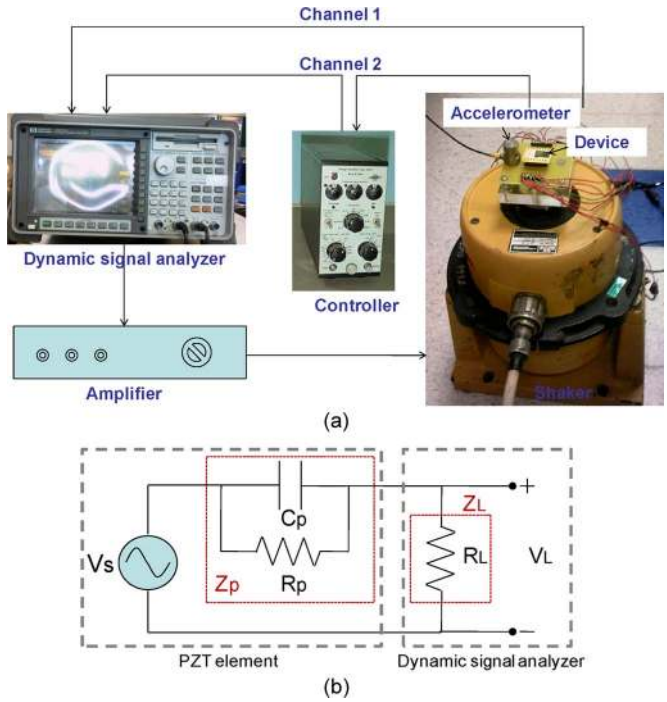

Fig. 4. (a) Vibration testing system for load voltage measurement and (b) its equivalent circuit for single PZT element.

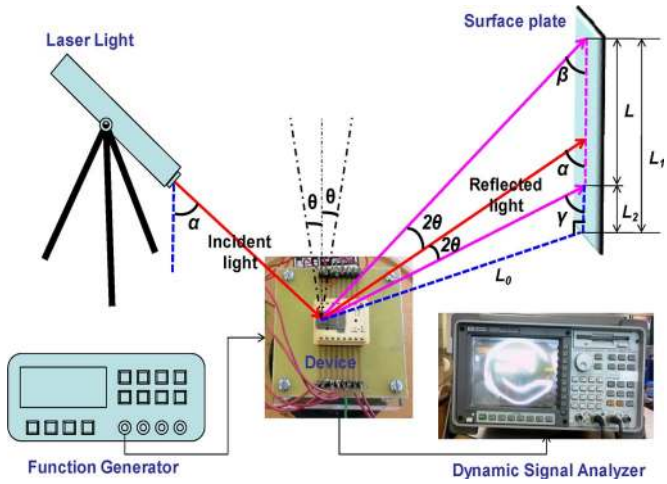

Fig. 5. Optical setup for the measurement of mass tip displacement.

Because the piezoelectric cantilever contains 10 PZT elements, some PZT elements can be used as PZT actuators and the others are used as PZT EHs. As the PZT actuators excited by the AC voltage generated from the function generator, the piezoelectric cantilever starts to oscillate. Subsequently, the PZT EHs will generate electrical voltage due to the self-oscillation of the cantilever. The bending angle of the cantilever can be derived from the sweeping distance of the reflected light on the surface plate.

To calculate such relationship, the radius of curvature of the bending beam is assumed constant, and the initial bending angle is assumed to be zero. The incident light illuminates onto the mass surface with a fixed angle of a and is reflected on the surface plate with the same angle. Within one vibration cycle, the cantilever deflects clockwise and anticlockwise with

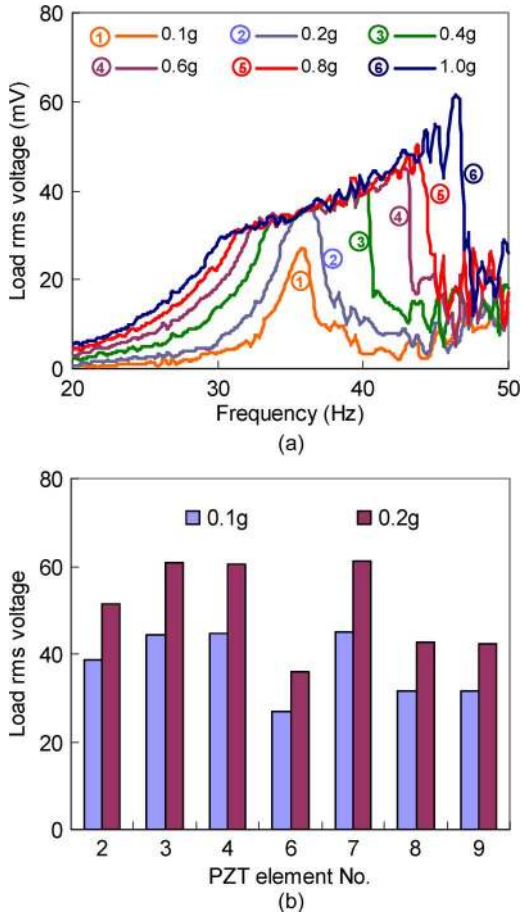

Fig. 6. (a) Load rms voltages against frequencies for No. 6 PZT element at different accelerations. (b) Load rms voltages at resonant frequency for each individual PZT element at accelerations of 0.1 g and 0.2 g.

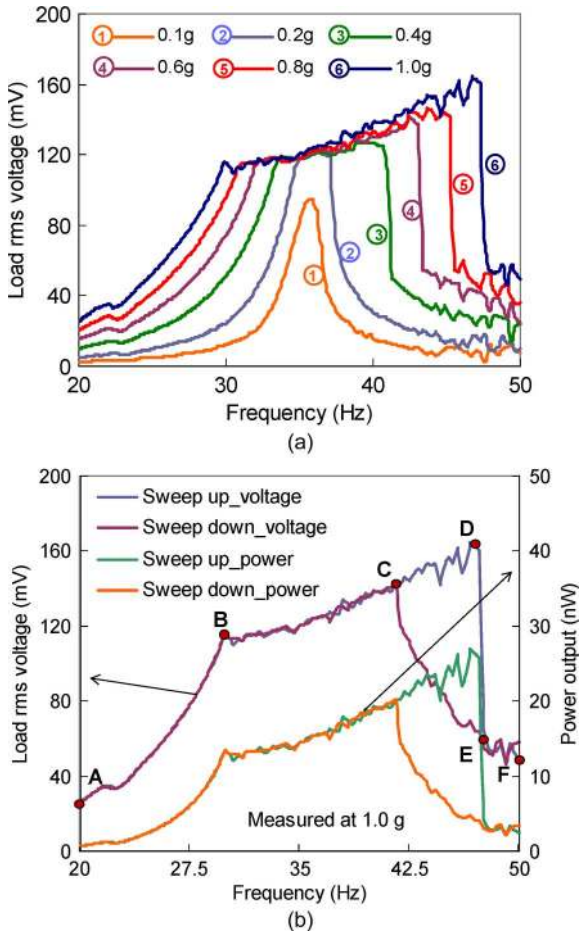

Fig. 7. (a) Load rms voltages against frequencies for six PZT elements in parallel connection at different accelerations. (b) Load rms voltages and power outputs against frequencies for six PZT elements in parallel connection at accelerations of 1.0 g by frequency sweeping up and down.

angle of θ, and the reflected light sweeps up and down from the original reflection light with angle of 2θ. The maximum sweeping distance L can be measured during vibration and can be expressed as

$$L = L_1 - L_2 = \frac{L_0}{\tan(\beta)} - \frac{L_0}{\tan(\gamma)} \tag{9}$$

where the reflection angle β and γ can be expressed by incidence angle α and deflection angle θ of the cantilever as $\beta = \alpha - 2\theta$ and $\gamma = \alpha + 2\theta$, respectively. L_0 is the distance between the cantilever and surface plate. Therefore, the relationship between the deflection angle of the cantilever and sweeping distance can be express as

$$L = L_0 \left[\frac{1}{\tan(\alpha - 2\theta)} - \frac{1}{\tan(\alpha + 2\theta)} \right]. \tag{10}$$

Based on the deflection angle, the mass tip displacement can be obtained subsequently as

$$\delta_m = l_b(1 - \cos\theta)/\sin\theta + l_m \sin\theta. \tag{11}$$

B. Low and Wideband Operation Frequency

The vibration testing system was used to characterize the vibration behavior and energy harvesting performance of the piezoelectric cantilever. The piezoelectric cantilever was assembled onto a PCB board and six of the ten PZT elements were individually connected to the DSA for load voltage measurement. The input acceleration was applied by the vibration shaker to the cantilever device. As the vibration frequency of the shaker swept from 20 Hz to 50 Hz, the load voltages generated from each single PZT element were recorded to the DSA. Fig. 6(a) shows the load rms voltages of No. 6 PZT element against vibration frequencies under different input accelerations ranging from 0.1 g, 0.2 g, 0.4 g, 0.6 g, 0.8 g to 1.0 g, respectively. It is found that at low input acceleration of 0.1 g, the maximum load rms voltage of 27 mV is generated at a quite low resonant frequency of 36 Hz. As the input acceleration raises higher than 0.2 g, the load rms voltage will be suppressed but the operation frequency will be extended to a wider bandwidth around the original resonant frequency, i.e., 36 Hz. The higher input acceleration, the wider bandwidth of the operation frequency. Actually, the other PZT elements were also measured in the same way and the load rms voltages showed similar trends as No. 6 PZT element but with higher output voltages. Fig. 6(b) shows that the load rms voltages for individual PZT element at 0.1 g and 0.2 g fluctuate, and the average load rms voltages with respect to resistance of 1 MΩ are 37 mV and 50 mV at 0.1 g and 0.2 g, respectively. Because these

TABLE I
OPERATION FREQUENCY BANDWIDTH COMPARISON BETWEEN THIS WORK AND PUBLISHED WIDEBAND EHS

Ref.	Approach	Device	Acceleration (g)	Freq. bandwidth (Hz)	Center freq. (Hz)	Normalized freq. bandwidth
[42]	Cantilever array	--	--	87 -115	100	0.28
[43]	Cantilever array	MEMS	50	4200 - 5000	4600	0.17
[45]	Mechanical stopper	Prototype	0.1	94 - 99	94.7	0.05
[46]	Nonlinear spring	MEMS	0.158	520 - 590	588	0.12
This work	Amplitude limitation mechanism	MEMS	1.0	30 – 47	36	0.47

ten PZT elements parallel-arrayed on the supporting beam, as long as the supporting beam deflects in each vibrate cycle, the ten PZT elements experience the same strain distribution in each cycle. Therefore, the voltage output fluctuation of individual PZT element may be due to the small variation of the PZT dimension in fabrication steps.

Fig. 7(a) shows the load rms voltages against vibration frequencies for six PZT elements (No. 2, 3, 4, 7, 8, and 9) connected in parallel at different input accelerations. It shows the similar trend of wideband effect as single PZT element in Fig. 6(a), but with much higher voltage output. For input acceleration of 0.1 g, the maximum load rms voltage is 94 mV at the same resonant frequency of 36 Hz. As the input acceleration comes to 1.0 g, the load rms voltages can achieve 114 mV, 124 mV, and 164 mV at frequencies of 30.1 Hz, 36 Hz, and 47.3 Hz, respectively. As seen from Figs. 6(a) and 7(a), for an input acceleration of 1.0 g, the operation frequency bandwidth is able to extend as broad as 17 Hz (from 30 Hz to 47 Hz). Meanwhile, the load rms voltage is steadily increased within this frequency bandwidth of 17 Hz. These figures also indicate that as long as the vibration frequencies are within this frequency range, the load rms voltage will remain constant at different input accelerations.

Such wideband effect is realized by having a predetermined spacer thickness between the piezoelectric cantilever and carrier base as demonstrated in Section II-A. Taken six PZT elements with an input acceleration of 1.0 g for example [shown in Fig. 7(b)], by increasing the excitation frequency from 20 Hz, the load rms voltage increased monotonically from point A until point B (30 Hz), and the proof mass hit the carrier base at this moment. The increasing rate of the load rms voltage decreased until it reached point D (47 Hz) where the load rms voltage suddenly and dramatically decreased to point E, at which the system was linear and no more rattling occurred. From point E to point F, load rms voltage decreased by increasing the excitation frequency until 50 Hz. As the excitation frequency swept down from 50 Hz, the load rms voltage increased through point F to point C (41.5 Hz), where again the moving mass hit the carrier base and the rattling occurred. By decreasing the excitation frequency to point B, the mass stopped hitting the carrier base, and the load rms voltage decreased from point B to point A at 20 Hz. As a result, the operation frequency bandwidth is greatly widened from 11.5 Hz to 17 Hz, which is nearly 150% of the original bandwidth. Based on the measured load rms voltage at 1.0 g, the power output was calculated and plotted in the same figure with respect to 1 MΩ load resistance. As seen from Fig. 7(b), both the load rms voltage and power output show a steady increment and wideband output range. Within the operation frequency bandwidth from 30 Hz to 47 Hz, the power output gradually varies from 13 nW to 27 nW. The operation bandwidth of this piezoelectric EH device is compared with the published wideband EHs in Table I. In terms of normalized frequency bandwidth (NFB), which is obtained by operation frequency bandwidth divided by center operation frequency, the proposed piezoelectric EH device realized much higher NFB than reported EH devices.

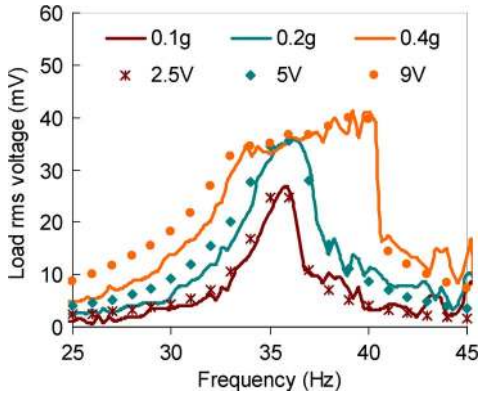

Fig. 8. Calibration of the load rms voltages of No. 6 PZT element against frequencies at various AC excitation voltages and input accelerations.

C. Mass Tip Displacement and Voltage Generation

To demonstrate the wideband effect of the proposed EH device and to figure out the relationship between mass tip displacement and voltage output, the optical setup shown in Fig. 5 was used. In the experiment, the function generator was connected with six PZT elements (No. 2, 3, 4, 7, 8, and 9) in parallel, as the AC excitation voltage source. The PZT element of No. 6 was connected with the DSA as the energy harvesting element. The excitation frequencies were set manually from 25 Hz to 45 Hz with interval of 1 Hz, and the AC excitation voltages were applied from 1 V to 10 V with interval of 0.5 V. Fig. 8 shows the calibration of the load rms voltages of No. 6 PZT element against frequencies at different AC excitation voltages in comparison with the voltage outputs at corresponding input accelerations. It indicates that the voltage outputs and vibration behaviors of the piezoelectric cantilever excited by six PZT elements at AC excitation voltages of 2.5 V, 5 V, and 9 V are equivalent as the piezoelectric cantilever excited by input accelerations of 0.1 g, 0.2 g, and 0.4 g, respectively.

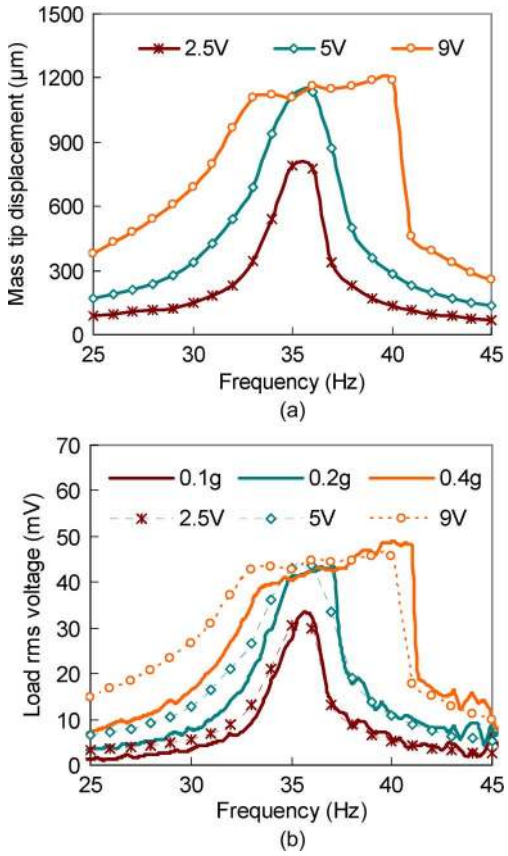

Fig. 9. (a) Mass tip displacements against frequencies at different AC self-excitation voltages. (b) Experimental and theoretical results of the load rms voltages against frequencies for No. 9 PZT element.

Under the same AC excitation voltages of 2.5 V, 5 V and 9 V, the sweeping distances of reflected laser light on the surface plate were measured against frequencies from 25 Hz to 45 Hz. By using (10) and (11), the mass tip displacement can be calculated from the measured sweeping distances and plotted in Fig. 9(a). In the figure, at the AC excitation voltage of 5 V which is equivalent as input acceleration of 0.2 g, the maximum mass tip displacement arrived at 1150 μm, which was just the space distance between the bottom surface of the mass tip and the carrier base. By raising the AC excitation voltage to 9 V, as the excitation frequency increased from 25 Hz, the mass tip displacement raised monotonically from 381 μm until hitting of the carrier base at 33 Hz. After that, the moving mass started rattling with the carrier base until vibration frequency reached 40 Hz, where the moving mass displacement suddenly and dramatically decreased from 1150 μm to 458 μm. The mass displacement was linearly decreased to 260 μm at 45 Hz without any rattling occurred.

Based on the experimental results of mass tip displacement, the output voltages of single PZT element can be calculated according to (6). Table II lists the material properties and structural parameters of the piezoelectric cantilever used in the calculation. The theoretical results are compared with experimental voltage outputs of No. 9 PZT element, which has an average output among these PZT elements. As shown in Fig. 9(b), the results match well, where solid curves are the experimental results by using vibration shaker excited at 0.1 g, 0.2 g, and 0.4 g, and dotted curves are the calculated voltage outputs by the measured mass tip displacements at AC excitation voltage of 2.5 V, 5 V, and 9 V.

TABLE II
MATERIAL PROPERTIES AND STRUCTURAL PARAMETERS OF THE PIEZOELECTRIC CANTILEVERS

Parameters	Description	Value
d_{31}	Transverse piezoelectric constant	-50 pm V^{-1}
Y	Young's modulus of PZT	72 GPa
ε_0	Vacuum dielectric constant	8.85e-12 Fm^{-1}
$\varepsilon_{33}/\varepsilon_0$	Relative dielectric constant of PZT	1000
w_e	Width of individual PZT element	0.24 mm
w	Width of the cantilever beam	5 mm
l_e	Length of individual PZT element	3.26 mm
l_b	Length of supporting beam	3 mm
l_m	Length of proof mass	5 mm
t_e	Thickness of PZT layer	2.95 μm
t_b	Thickness of supporting beam	5 μm
δ_m	Mass tip displacement (Max.)	1.15 mm

IV. SERIES AND PARALLEL CONNECTION

A. Voltage Outputs for PZT Elements Connected in Series and in Parallel

For the comparison of PZT elements connected in series and in parallel, load rms voltages were measured by using vibration testing system in Fig. 4(a). The input impedance 1 MΩ of DSA was served as the load resistance in the testing and following discussion. Fig. 10(a) and (b) show the load rms voltages against frequencies for gradually increasing numbers of PZT elements connected in series at accelerations of 0.1 g and 0.2 g, respectively. Likewise, Fig. 11(a) and (b) show the load rms voltages against frequencies for varying numbers of PZT elements connected in parallel at accelerations of 0.1 g and 0.2 g. For example, "S234987" indicates PZT elements of No. 2, 3, 4, 9, 8, and 7 connected in series and "P234987" means PZT elements of No. 2, 3, 4, 9, 8, and 7 connected in parallel. It is found that the load rms voltages for series connection overlap with each other and are not affected by the numbers of PZT elements. However, for parallel connection, as the numbers of PZT elements gradually increase from one to six, the load rms voltages increase. As seen in Fig. 11, the maximum voltage peaks of 94 mV and 119 mV occur at the resonant frequency of 36 Hz with input accelerations of 0.1 g and 0.2 g, respectively.

From Figs. 10 and 11, the voltage peaks at resonant frequency of 36 Hz for different numbers of PZT elements connected in series and in parallel are extracted and shown in Fig. 12(a). The trend difference can be seen more clearly in Fig. 12(a). For series connection, the load rms voltage remains relatively constant regarding the gradually increasing numbers of PZT elements. However, for parallel connection, the

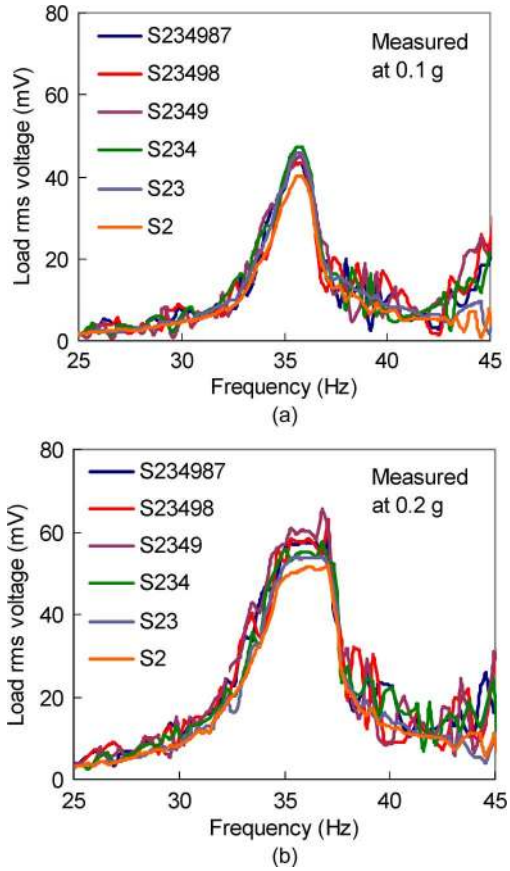

Fig. 10. Load rms voltages against frequencies for gradually increasing numbers of PZT elements connected in series at accelerations of 0.1 g (a) and 0.2 g (b).

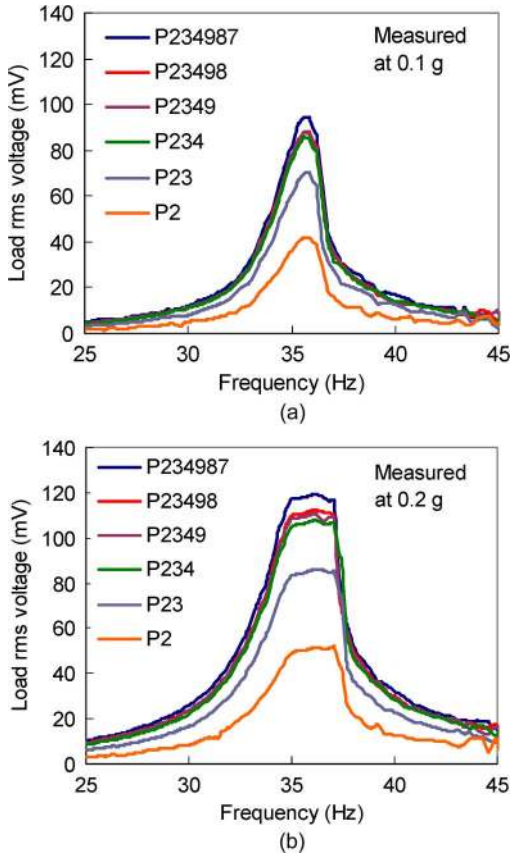

Fig. 11. Load rms voltages against frequencies for gradually increasing numbers of PZT elements connected in parallel at accelerations of 0.1 g (a) and 0.2 g (b).

load rms voltage raises with the increment of connected PZT elements. The raising rate of the load rms voltage decreases until relatively constant with the increment of PZT elements. Such voltage trends for series and parallel connections are due to the large PZT impedance. It is known that, for n voltage sources connected in series, the resultant voltage is n times larger than single voltage source. However, the resultant impedance is also n times larger than the impedance of single voltage source (here refers to PZT element). Therefore, the load voltage delivered to the external impedance which is smaller than the impedance of single PZT element does not change much. For n voltage sources connected in parallel, the resultant voltage is the same as single voltage source. Meanwhile, the resultant impedance is 1/n times smaller than the impedance of single PZT element. Therefore, initially, the load voltage delivered to the external impedance will increase greatly, but gradually remain constant as increasing numbers of voltage sources connected. Such trends can be explained and verified by using simulation software SPICE as shown in Fig. 12(b). In the simulation, the source voltage Vs of each PZT element is derived from the measured load rms voltage V_L in Fig. 6(b) by using equivalent circuit as shown in Fig. 4(b). It is found that the simulation results match quite well with the experimental results. The minor difference is because the fluctuation of the impedance of each PZT element was not considered in the simulation.

B. Power Outputs for PZT Elements Connected in Series and in Parallel

In Figs. 13 and 14, the load rms voltages and corresponding power outputs are presented regarding varying resistances by experimental and simulation methods. In the experiment, load resistors in parallel with DSA were connected with six PZT elements in series and in parallel connections. Thus, the load rms voltage measured by the DSA was referring to the resultant resistance of the external resistors and internal impedance of the DSA connected in parallel.

Fig. 13(a) and (b) show the experimental results of load rms voltages and power outputs against load resistances for six PZT elements connected in series at accelerations of 0.1 g and 0.2 g. It is seen that the load rms voltages and power outputs increase monotonically. Be noted that the load resistance range is within 800 KΩ, because the impedance of DSA is 1 MΩ, the resultant load resistance will always be smaller than 1 MΩ, no matter how large the external resistors of the circuit connected with. It is also known that the maximum power output occurs when the load impedance matches with the resultant internal impedance of the PZT elements in the circuit. For six PZT elements connected in series, the resultant impedance is too large that beyond the measurement range. Therefore, in Fig. 13(b), it is only seen a gradually growing power output without appearing a maximum power peak. To complete and present the whole curve, simulation results by SPICE are shown in Fig. 13(c) and (d).

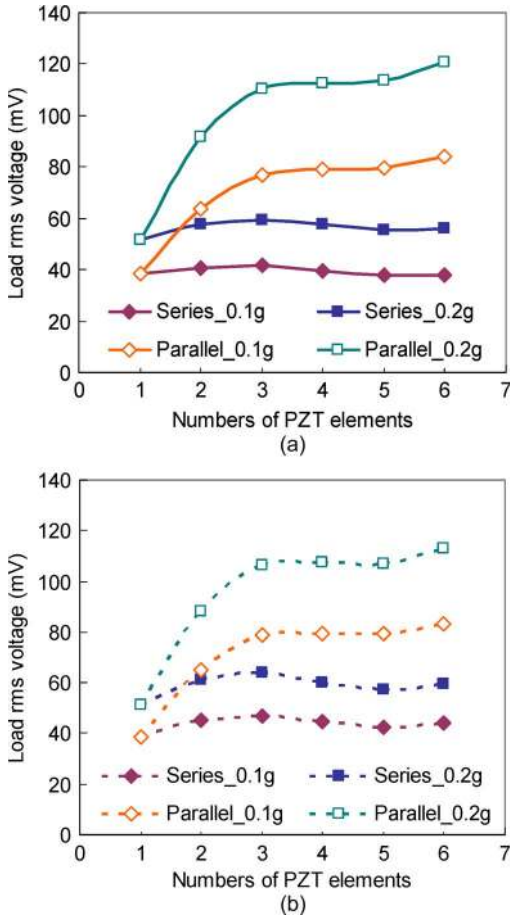

Fig. 12. (a) Experimental and (b) simulation results of voltage peaks at resonant frequency for different numbers of PZT elements connected in series and in parallel.

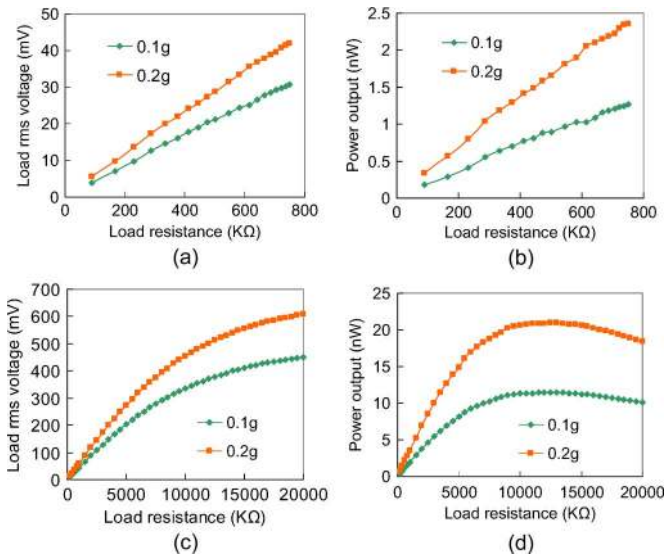

Fig. 13. Experimental results of load rms voltages (a) and power outputs (b) against load resistances for six PZT elements in series connection; simulation results of load rms voltages (c) and power outputs (d) against load resistances for six PZT elements in series connection.

It is seen that the load rms voltages tend toward constant values after monotonically increasing. The power outputs reach the maximum values of 11.4 nW and 20.9 nW with the matched load resistance of 12.5 MΩ at 0.1 g and 0.2 g, respectively.

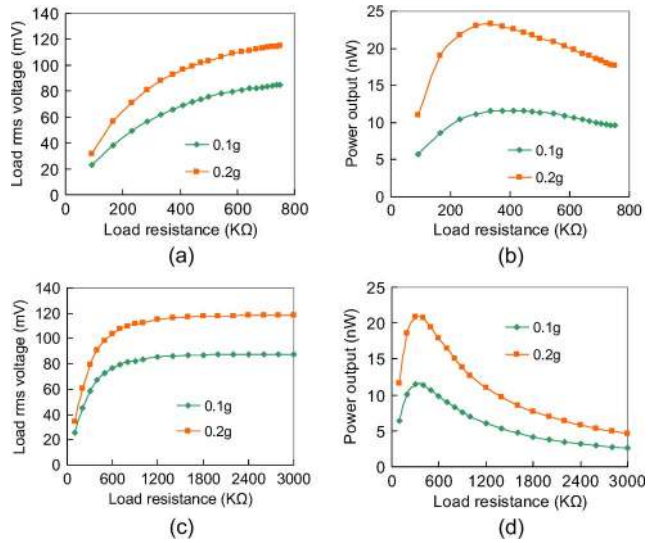

Fig. 14. Experimental results of load rms voltages (a) and power outputs (b) against load resistances for six PZT elements in parallel connection; simulation results of load rms voltages (c) and power outputs (d) against load resistances for six PZT elements in parallel connection.

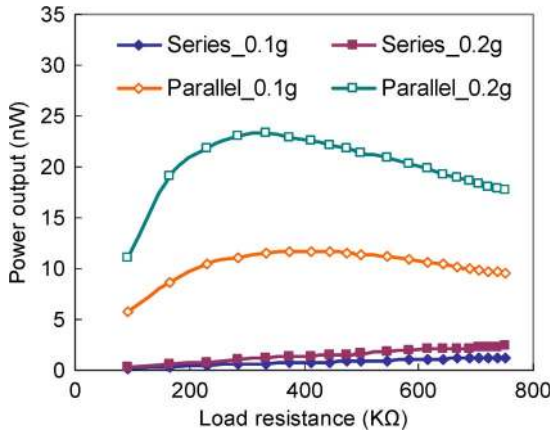

Fig. 15. Comparison of power outputs for PZT elements in series and in parallel connections.

For six PZT elements connected in parallel, Fig. 14(a) and (b) show the experimental results of load rms voltages and power outputs against load resistances at accelerations of 0.1 g and 0.2 g. It is seen that the load rms voltage increases monotonically as the load resistance increases. Nevertheless, the power outputs reach the peak values of 11.6 nW and 23.3 nW with matched resistance of 333 KΩ at 0.1 g and 0.2 g. The simulation results are shown in Fig. 14(c) and (d). Similarly, the slope of the curve of the load rms voltage tends to be gradually reduced after the load resistance continuously increased above the value of the load resistance at maximum output power. Moreover, the power outputs reach the maximum values of 11.6 nW and 23.3 nW which are in the same level as the values of 11.4 nW and 20.9 nW for six PZT elements in series connection in Fig. 13(c) and (d) at the accelerations of 0.1 g and 0.2 g, but with a quite small matched load resistance of 330 KΩ. Thus, it is concluded that, in spite of the connection types of these PZT elements, the optimal power

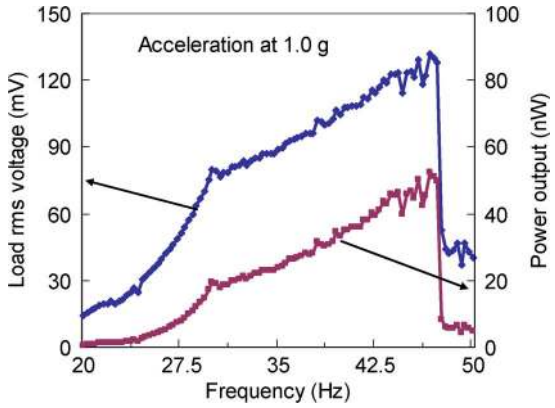

Fig. 16. Load rms voltage and power output of six PZT elements connected in parallel with respect to load resistance of 330 KΩ.

generated for six PZT elements remains the same with respect to corresponding matched load resistance.

Combining the experimental results from Figs. 13(b) and 14(b), the power outputs against load resistances are rearranged and shown in Fig. 15. Although PZT elements connected in series and in parallel produce similar power into matched load resistance, the matched resistance in case of parallel is much lower than the one of series connection. Hence, it is concluded that PZT elements in parallel connection is preferred, because it produces much higher power output than the case of series connection under low load resistance. For this reason, the power generation for PZT elements in parallel connection will be further discussed in the next section.

V. Evaluation and Discussion of Power Generation

From the experimental results in Fig. 14(b), the optimal powers generated for six PZT elements in parallel connection at 0.1 g and 0.2 g are 11.6 nW and 23.3 nW. Thus, the optimal powers generated for single PZT element are 1.9 nW and 3.9 nW at 0.1 g and 0.2 g. Subsequently, for ten PZT elements connected in parallel, the optimal powers generated at the same input accelerations are calculated as 19.3 nW and 38.8 nW. When the input acceleration exceeds 0.2 g, it starts to show a wideband effect of voltage and power generations. Fig. 16 shows the derived results for load rms voltage and power output against frequency for six PZT elements connected in parallel with respect to load resistance of 330 KΩ at 1.0 g. Within the operation bandwidth from 30 Hz to 47 Hz, the load rms voltage gradually varies from 75.5 mV to 115.5 mV. Likewise, output power increases gradually from 19.4 nW to 51.3 nW. Subsequently, for ten PZT elements connected in parallel, the optimal powers generated at 1.0 g are calculated as 32.3 nW at 30 Hz and gradually increased as 85.5 nW at 47 Hz.

There might be three possible approaches for further increasing the power generation of such piezoelectric EH device. First, modify the dimension parameters of PZT elements. Here, the dimensions of the cantilever and lengths of PZT elements remain unchanged, so the vibration behavior of the cantilever maintains the same. Assuming we can only change the PZT layer thickness and width, since the optimal power is proportional to the width w_e and thickness t_e of PZT layer, the maximum power of such piezoelectric cantilever at 1.0 g would become 0.18 μW under a much lower matched impedance of 42 KΩ, by having the PZT pattern covering the whole supporting beam. Thus, the power density for such device is 11 μW/cm^3. Second, the spacer thickness between cantilever and carrier base can be adjusted to realize larger vibration amplitude of the cantilever and then larger power output. According to simulation, if the spacer is increased from 1.15 mm to 2 mm, the critical acceleration to realize such vibration amplitude of 2 mm would be 0.3 g. Once the acceleration is more than 0.3 g, it will also show a wideband voltage and power output. In this case, the maximum power obtained at 1.0 g would be around 0.53 μW. Then, the power density for this device would be 33 μW/cm^3. Last but the most important factor which leads to low output power is the quite low resonant frequency of the piezoelectric EH device. Operating at high resonant frequency will result in a low impedance of PZT element and then high power output. However, this is not suitable for most practical applications which have low environmental vibration frequencies. One reasonable solution is to employ frequency-up-conversion mechanism [54], [55] which converts low-frequency ambient vibrations into high frequency vibrations to improve the power generation for such MEMS piezoelectric EH device at low operation frequency.

VI. Conclusion

This paper has demonstrated the design, fabrication, and characterization of a MEMS-based piezoelectric EH device operating at a quite low resonant frequency with a wideband operation range. In this design, a Si proof mass is integrated with the piezoelectric beam to realize a resonant frequency as low as 36 Hz. By adjusting the spacer thickness, the vibration behavior of the cantilever is limited in amplitude domain but extended in frequency domain. Due to the wideband effect, the voltage and power generations show a steadily increased and wideband range once the critical input acceleration of 0.2 g is exceeded. As a result, for input acceleration of 1.0 g, the operation frequency bandwidth is obtained as 17 Hz which is as large as 0.47 in terms of NFB. Such stable and wideband output will benefit the future design of energy harvesting and storage circuit. To optimize the output power, six PZT elements connected in series and in parallel are compared and discussed. It is found that, under the same input acceleration, the optimal power remains the same no matter what the connection type is. However, the impedance measured at the maximum output power is reduced by connecting PZT elements in parallel. Finally, the voltage and power generations for PZT elements in parallel connection are evaluated and discussed. It shows that, by integrating ten PZT elements in parallel, the power generated at 1.0 g with respect to load resistance of 330 KΩ is able to achieve a wideband output ranging from 32.3 nW to 85.5 nW within the operation bandwidth from 30 Hz to 47 Hz. Feasible approaches are proposed to improve the power generation further. By having the PZT pattern covering the whole supporting beam and increasing the spacer thickness up to 2 mm, theoretical calculation shows that the maximum power

and power density at an acceleration of 1.0 g would be around 0.53 μW and 33 μW/cm^3, respectively.

REFERENCES

[1] T. Starner, "Human-powered wearable computing," *IBM Syst. J.*, vol. 35, no. 3/4, pp. 618–629, 1996.

[2] S. Roundy, P. K. Wright, and J. Rabaey, "A study of low level vibrations as a power source for wireless sensor nodes," *Comput. Commun.*, vol. 26, no. 11, pp. 1131–1144, Jul. 2003.

[3] S. P. Beeby, M. J. Tudor, and N. M. White, "Energy harvesting vibration sources for microsystems applications," *Meas. Sci. Technol.*, vol. 17, no. 12, pp. 175–195, Dec. 2006.

[4] P. D. Mitcheson, E. M. Yeatman, G. K. Rao, A. S. Holmes, and T. C. Green, "Energy harvesting from human and machine motion for wireless electronic devices," *Proc. IEEE*, vol. 96, no. 9, pp. 1457–1486, Sep. 2008.

[5] S. Roundy and P. K. Wright, "A piezoelectric vibration based generator for wireless electronics," *Smart Mater. Struct.*, vol. 13, no. 5, pp. 1131–1142, Oct. 2004.

[6] S. Kulkarni, E. Koukharenko, R. Torah, J. Tudor, S. Beeby, T. O'Donnell, and S. Roy, "Design, fabrication and test of integrated micro-scale vibration-based electromagnetic generator," *Sens. Actuators A, Phys.*, vol. 145–146, no. 1/2, pp. 336–342, Jul./Aug. 2008.

[7] B. Yang, C. Lee, W. Xiang, J. Xie, J. H. He, R. K. Kotlanka, S. P. Low, and H. Feng, "Electromagnetic energy harvesting from vibrations of multiple frequencies," *J. Micromech. Microeng.*, vol. 19, no. 3, pp. 035 001-1–035 001-8, Mar. 2009.

[8] Y. Sakane, Y. Suzuki, and N. Kasagi, "Development of high-performance perfuluoriented polymer electret film and its application to micro power generation," *J. Micromech. Microeng.*, vol. 18, no. 10, pp. 104 011-1–104 011-6, Oct. 2008.

[9] M. Edamoto, Y. Suzuki, N. Kasagi, K. Kashiwagi, Y. Morizawa, T. Yokoyama, T. Seki, and M. Oba, "Low-resonant-frequency micro electret generator for energy harvesting application," in *Proc. 22nd IEEE Int. Conf. MEMS*, 2009, pp. 1059–1062.

[10] B. Yang, C. Lee, W. L. Kee, and S. P. Lim, "Hybrid energy harvester based on piezoelectric and electromagnetic mechanisms," *J. Micro/Nanolith. MEMS MOEMS*, vol. 9, no. 2, pp. 023 002-1–023 002-10, Apr. 2010.

[11] S. Tadigadapa and K. Mateti, "Piezoelectric MEMS sensors: State-of-the-art and perspectives," *Meas. Sci. Technol.*, vol. 20, no. 9, pp. 092 001-1–092 001-30, Sep. 2009.

[12] P. D. Mitcheson, E. K. Reilly, T. Toh, P. K. Wright, and E. M. Yeatman, "Performance limits of the three MEMS inertial energy generator transduction types," *J. Micromech. Microeng.*, vol. 17, no. 9, pp. S211–S216, 2007.

[13] S. R. Anton and H. A. Sodano, "A review of power harvesting using piezoelectric materials (2003–2006)," *Smart Mater. Struct.*, vol. 16, no. 3, pp. R1–R21, Jun. 2007.

[14] K. A. Cook-Chennault, N. Thambi, and A. M. Sastry, "Powering MEMS portable devices—A review of non-regenerative and regenerative power supply systems with special emphasis on piezoelectric energy harvesting systems," *Smart Mater. Struct.*, vol. 17, no. 4, pp. 043 001-1–043 001-33, Aug. 2008.

[15] S. Saadon and O. Sidek, "A review of vibration-based MEMS piezoelectric energy harvesters," *Energy Convers. Manage.*, vol. 52, no. 1, pp. 500–504, Jan. 2011.

[16] S. Jiang, X. Li, S. Guo, Y. Hu, J. Yang, and J. Qing, "Performance of a piezoelectric bimorph for scavenging vibration energy," *Smart Mater. Struct.*, vol. 14, no. 4, pp. 769–774, Aug. 2005.

[17] S. Roundy, E. S. Leland, J. Baker, E. Carleton, E. Reilly, E. Lai, B. Otis, J. M. Rabaey, P. K. Wright, and V. Sundararajan, "Improving power output for vibration-based energy scavengers," *IEEE Pervasive Comput.*, vol. 4, no. 1, pp. 28–36, Jan.–Mar. 2005.

[18] Y. C. Shu and I. C. Lien, "Analysis of power output for piezoelectric energy harvesting systems," *Smart Mater. Struct.*, vol. 15, no. 6, pp. 1499–1512, Dec. 2006.

[19] J. Ajitsaria, S. Y. Choe, D. Shen, and D. J. Kim, "Modeling and analysis of a bimorph piezoelectric cantilever beam for voltage generation systems," *Smart Mater. Struct.*, vol. 16, no. 2, pp. 447–454, Apr. 2007.

[20] A. Erturk and D. J. Inman, "An experimentally validated bimorph cantilever model for piezoelectric energy harvesting from base excitations," *Smart Mater. Struct.*, vol. 18, no. 2, pp. 025 009-1–025 009-18, Feb. 2009.

[21] T. M. Kamal, R. Elfrink, M. Renaud, D. Hohlfeld, M. Goedbloed, C. de Nooijer, M. Jambunathan, and R. van Schaijk, "Modeling and characterization of MEMS-based piezoelectric harvesting devices," *J. Micromech. Microeng.*, vol. 20, no. 10, pp. 105 023-1–105 023-14, Oct. 2010.

[22] J. C. Park, J. Y. Park, and Y. P. Lee, "Modeling and characterization of piezoelectric d33-mode MEMS energy harvester," *J. Microelectromech. Syst.*, vol. 19, no. 5, pp. 1215–1222, Oct. 2010.

[23] C. B. Williams and R. B. Yates, "Analysis of a micro-electric generator for microsystems," *Sens. Actuators A, Phys.*, vol. 52, no. 1–3, pp. 8–11, Mar./Apr. 1996.

[24] Y. B. Jeon, R. Sood, J. H. Jeong, and S. G. Kim, "MEMS power generator with transverse mode thin film PZT," *Sens. Actuators A, Phys.*, vol. 122, no. 1, pp. 16–22, Jul. 2005.

[25] H. B. Fang, J. Q. Liu, Z. Y. Xu, L. Dong, L. Wang, D. Chen, B. C. Cai, and Y. Liu, "Fabrication and performance of MEMS-based piezoelectric power generator for vibration energy harvesting," *Microelectron. J.*, vol. 37, no. 11, pp. 1280–1284, Nov. 2006.

[26] W. J. Choi, Y. Jeon, J. H. Jeong, R. Sood, and S. G. Kim, "Energy harvesting MEMS device based on thin film piezoelectric cantilevers," *J. Electroceram.*, vol. 17, no. 2–4, pp. 543–548, Dec. 2006.

[27] D. Shen, J. H. Park, J. Ajitsaria, S. Y. Choe, H. C. Wikle, and D. J. Kim, "The design, fabrication and evaluation of a MEMS PZT cantilever with an integrated Si proof mass for vibration energy harvesting," *J. Micromech. Microeng.*, vol. 18, no. 5, pp. 055 017-1–055 017-7, May 2008.

[28] J. Q. Liu, H. B. Fang, Z. Y. Xu, X. H. Mao, X. C. Shen, D. Chen, H. Liao, and B. C. Cai, "A MEMS-based piezoelectric power generator array for vibration energy harvesting," *Microelectron. J.*, vol. 39, no. 5, pp. 802–806, May 2008.

[29] M. Renaud, K. Karakaya, T. Sterken, P. Fiorini, C. Van Hoof, and R. Puers, "Fabrication, modeling and characterization of MEMS piezoelectric vibration harvesters," *Sens. Actuators A, Phys.*, vol. 145/146, no. 1/2, pp. 380–386, Jul./Aug. 2008.

[30] M. Marzencki, Y. Ammar, and S. Basrour, "Integrated power harvesting system including a MEMS generator and a power management circuit," *Sens. Actuators A, Phys.*, vol. 145/146, no. 1/2, pp. 363–370, Jul./Aug. 2008.

[31] B. S. Lee, S. C. Lin, W. J. Wu, X. Y. Wang, P. Z. Chang, and C. K. Lee, "Piezoelectric MEMS generators fabricated with an aerosol deposition PZT thin film," *J. Micromech. Microeng.*, vol. 19, no. 6, pp. 065 014-1–065 014-8, Jun. 2009.

[32] P. Muralt, M. Marzencki, B. Belgacem, F. Calame, and S. Basrour, "Vibration energy harvesting with PZT micro device," *Procedia Chem.*, vol. 1, no. 1, pp. 1191–1194, Sep. 2009.

[33] R. Elfrink, T. M. Kamel, M. Goedbloed, S. Matova, D. Hohlfeld, Y. van Andel, and R. van Schaijk, "Vibration energy harvesting with aluminum nitride-based piezoelectric devices," *J. Micromech. Microeng.*, vol. 19, no. 9, pp. 094 005-1–094 005-8, Sep. 2009.

[34] E. K. Reilly and P. K. Wright, "Modeling, fabrication and stress compensation of an epitaxial thin film piezoelectric microscale energy scavenging device," *J. Micromech. Microeng.*, vol. 19, no. 9, pp. 095 014-1–095 014-11, Sep. 2009.

[35] D. Zhu, M. J. Tudor, and S. P. Beeby, "Strategies for increasing the operating frequency range of vibration energy harvesters: A review," *Meas. Sci. Technol.*, vol. 21, no. 2, pp. 022 001-1–022 001-29, Feb. 2010.

[36] J. J. Yao and N. C. MacDonald, "A micromachined, single-crystal silicon, tunable resonator," *J. Micromech. Microeng.*, vol. 5, no. 3, pp. 257–264, Sep. 1995.

[37] T. Remtema and L. Lin, "Active frequency tuning for micro resonator by localized thermal stressing effects," *Sens. Actuators A, Phys.*, vol. 91, no. 3, pp. 326–332, Jul. 2001.

[38] E. S. Leland and P. K. Wright, "Resonance tuning of piezoelectric vibration energy scavenging generators using compressive axial preload," *Smart Mater. Struct.*, vol. 15, no. 5, pp. 1413–1420, Oct. 2006.

[39] C. Eichhorn, F. Goldschmidtboeing, and P. Woias, "A frequency piezoelectric energy convert based on a cantilever beam," in *Proc. PowerMEMS + microEMS*, Sendai, Japan, Nov. 9–12, 2008, pp. 309–312.

[40] X. Wu, J. Lin, S. Kato, K. Zhang, T. Ren, and L. Liu, "A frequency adjustable vibration energy harvester," in *Proc. PowerMEMS + microEMS*, Sendai, Japan, Nov. 9–12, 2008, pp. 245–248.

[41] V. R. Challa, M. G. Prasad, Y. Shi, and F. T. Fisher, "A vibration energy harvesting device with bidirectional resonance frequency tunability," *Smart Mater. Struct.*, vol. 17, no. 1, pp. 015 035-1–015 035-10, Feb. 2008.

[42] H. Xue, Y. Hu, and Q. M. Wang, "Broadband piezoelectric energy harvesting devices using multiple bimorphs with different operating frequencies," *IEEE Trans. Ultrason., Ferroelectr., Freq. Control*, vol. 55, no. 9, pp. 2104–2108, Sep. 2008.

[43] I. Sari, T. Balkan, and H. Kulah, "An electromagnetic micro power generator for wideband environmental vibrations," *Sens. Actuators A, Phys.*, vol. 145/146, no. 1/2, pp. 405–413, Jul./Aug. 2008.
[44] M. S. M. Soliman, E. M. Abdel-Rahman, E. F. El-Saadany, and R. R. Mansour, "A wideband vibration-based energy harvester," *J. Micromech. Microeng.*, vol. 18, no. 11, pp. 115 021-1–115 021-11, Nov. 2008.
[45] M. S. M. Soliman, E. M. Abdel-Rahman, E. F. El-Saadany, and R. R. Mansour, "A design procedure for wideband micropower generators," *J. Microelectromech. Syst.*, vol. 18, no. 6, pp. 1288–1299, Dec. 2009.
[46] D. S. Nguyen, E. Halvorsen, G. U. Jensen, and A. Vogl, "Fabrication and characterization of a wideband MEMS energy harvester utilizing nonlinear springs," *J. Micromech. Microeng.*, vol. 20, no. 12, pp. 125 009-1–125 009-11, Dec. 2010.
[47] B. Yang and C. Lee, "Non-resonant electromagnetic wideband energy harvesting mechanism for low frequency vibrations," *Microsyst. Technol.*, vol. 16, no. 6, pp. 961–966, Jun. 2010.
[48] A. Narimani, M. F. Golnaraghi, and G. N. Jazar, "Frequency response of a piecewise linear vibration isolator," *J. Vib. Control*, vol. 10, no. 12, pp. 1775–1794, Dec. 2004.
[49] M. Zhu, E. Worthington, and J. Njuguna, "Analyses of power output of piezoelectric energy-harvesting devices directly connected to a load resistor using a coupled piezoelectric-circuit finite element method," *IEEE Trans. Ultrason., Ferroelectr., Freq. Control*, vol. 56, no. 7, pp. 1309–1317, Jul. 2009.
[50] E. B. Tadmor and G. Kosa, "Electromechanical coupling correction for piezoelectric layered beams," *J. Microelectromech. Syst.*, vol. 12, no. 6, pp. 899–906, Dec. 2003.
[51] C. Lee, S. Kawano, T. Itoh, and T. Suga, "Characteristics of sol-gel derived PZT thin films with lead oxide cover layers and lead titanate interlayers," *J. Mater. Sci.*, vol. 31, no. 17, pp. 4559–4568, Jan. 1996.
[52] C. Lee, T. Itoh, R. Maeda, and T. Suga, "Characterization of micromachined piezoelectric PZT force sensors for dynamic scanning force microscopy," *Rev. Sci. Instrum.*, vol. 68, no. 5, pp. 2091–2100, May 1997.
[53] T. Kobayashi and R. Maeda, "Smart optical microscanner with piezoelectric resonator, sensor, and tuner using $Pb(Zr, Ti)O_3$ thin film," *Appl. Phys. Lett.*, vol. 90, no. 18, pp. 183 514-1–183 514-3, Apr. 2007.
[54] H. Kulah and K. Najafi, "Energy scavenging from low-frequency vibrations by using frequency up-conversion for wireless sensors applications," *IEEE Sensors J.*, vol. 8, no. 3, pp. 261–268, Mar. 2008.
[55] I. Sari, T. Balkan, and H. Kulah, "An electromagnetic micro power generator for low-frequency environmental vibrations based on the frequency upconversion technique," *J. Microelectromech. Syst.*, vol. 19, no. 1, pp. 14–27, Feb. 2010.

Huicong Liu received the B.S. and M.S. degrees from the Department of Mechanical Engineering, University of Science and Technology Beijing, Beijing, China, in 2006 and 2008, respectively. She is currently working toward the Ph.D. degree in the Department of Mechanical Engineering, National University of Singapore, Singapore.

Her research interest is the dynamic characterization of MEMS components, mainly on vibration-based MEMS energy harvesters.

Cho Jui Tay received the B.Sc. and Ph.D. degrees from the University of Strathclyde, Glasgow, U.K., in 1974 and 1979, respectively.

He is currently an Associate Professor with the National University of Singapore, Singapore. His research interests include experimental mechanics, optical techniques, and MEMS/NEMS. He has published widely in international journals and has coauthored and edited several book and book chapters. He has been involved in various editorial work and serves as a reviewer for 13 international journals and grant award agencies. He has delivered invited talks at various universities and research institutions. He holds several patents in the area of microcomponents fabrication.

Prof. Tay has won several research and best paper awards including the David Cargill Prize, U.K.

Chenggen Quan received the B.Eng. degree in mechanical engineering and the M.Eng. degree in optical engineering from Harbin Institute of Technology, Harbin, China, in 1982 and 1988, respectively, and the Ph.D. degree from Warwick University, Coventry, U.K., in 1992. His Ph.D. research involved the quantitative analysis of holographic interferograms using fast Fourier transform algorithms.

Before joining the National University of Singapore (NUS), Singapore, he was a Senior Engineer at the National Measurement Centre, Singapore Productivity and Standards Board. He is currently an Associate Professor in the Department of Mechanical Engineering, NUS. His research interests include laser-based measurement techniques, nondestructive testing, optical shape measurement, moiré interferometry for electronic packaging, and automatic fringe-pattern analysis.

Takeshi Kobayashi received the B.S. and M.S. degrees in materials science from The University of Tokyo, Tokyo, Japan, where he received the Ph.D.degree in materials science, in 2002.

He was a Researcher at the National Institute of Advanced Industrial Science and Technology, Tsukuba, Japan. His research interests include piezoelectric MEMS devices and their applications to wireless sensor networks. He has contributed to 40 international journal papers and 40 conference proceedings. Two of his publications have been selected as highlighted papers of the *Journal of Micromechanics and Microengineering*, in 2007 and 2008.

Chengkuo Lee (M'96) received the M.S. degree in materials science and engineering from National Tsing Hua University, Hsinchu, Taiwan, in 1991, the M.S. degree in industrial and system engineering from Rutgers University, New Brunswick, NJ, in 1993, and the Ph.D. degree in precision engineering from The University of Tokyo, Tokyo, Japan, in 1996.

He worked as a Foreign Researcher in the Nanometerscale Manufacturing Science Laboratory of the Research Center for Advanced Science and Technology, The University of Tokyo, from 1993 to 1996. He had also worked in the Mechanical Engineering Laboratory, Advanced Industrial Science and Technology (AIST), Ministry of International Trade and Industry (MITI), Japan, as a JST Research Fellow in 1996. Thereafter, he became a Senior Research Staff Member of the Microsystems Laboratory, Industrial Technology Research Institute, Hsinchu, Taiwan. In September 1997, he joined Metrodyne Microsystem Corporation, Hsinchu, Taiwan, and established the MEMS device division and the first micromachining laboratory for commercial purposes in Taiwan. He was the Manager of the MEMS device division between 1997 and 2000. He was an Adjunct Assistant Professor in the Electro-physics Department of National Chiao Tung University, Hsinchu, Taiwan, in 1998, and an Adjunct Assistant Professor in the Institute of Precision Engineering of National Chung Hsing University, Taichung, Taiwan, from 2001 to 2005. In August 2001, he cofounded Asia Pacific Microsystems, Inc., where he first became Vice President of R&D, before becoming Vice President of the optical communication business unit and Special Assistant to the Chief Executive Officer in charge of international business and technical marketing for the MEMS foundry service. From 2006 to 2009, he was a Senior Member of the Technical Staff at the Institute of Microelectronics, A-Star, Singapore. He has been an Assistant Professor in the Department of Electrical and Computer Engineering, National University of Singapore, Singapore, since December 2005. He is the coauthor of *Advanced MEMS Packaging* (McGraw-Hill, 2010). He has contributed to more than 140 international conference papers and extended abstracts and 90 peer-reviewed international journal articles in the fields of sensors, actuators, energy harvesting, NEMS, nanophotonics, and nanotechnology. He is also the holder of nine U.S. patents.